Inorganic Chemistry

ARTICLE

pubs.acs.org/IC

Crystal Structure and Morphology Evolution in the $LaXO_3$, X = Al, Ga, In Nano-Oxide Series. Consequences for the Synthesis of Luminescent Phosphors

Robert Pazik,*[,†] Gulaim A. Seisenbaeva,[†] Rafal J. Wiglusz,*[,‡] Leszek Kepinski,[‡] and Vadim G. Kessler[†]

[†]Department of Chemistry, SLU, P.O. Box 7015, 750 07 Uppsala, Sweden

[‡]Institute of Low Temperature and Structure Research, PAS, Okolna 2, 50-422 Wroclaw, Poland

ABSTRACT: The $LaXO_3$:Tb^{3+} (X = Al^{3+}, Ga^{3+}, In^{3+}) perovskite nanoparticles were obtained using the nonhydrolytic treatment (Bradley reaction) of the molecular precursors of the $La(O^iPr)_3$, $Al(O^iPr)_3$, $Ga(O^iPr)_3$, $In_5O(O^iPr)_{13}$, and $Tb(acac)_3$, respectively. It was shown that crystal structure and morphology evolution in the $LaXO_3$, X = Al, Ga, In nano-oxide series depended on the size and chemical properties of the X-metal atom. Formation of the $LaInO_3$:Tb^{3+} nanoparticles is distinctly less thermodynamically demanding on contrary to the $LaAlO_3$:Tb^{3+} and $LaGaO_3$:Tb^{3+} since it provided crystalline product directly in the solution synthesis at 202 °C, which is the lowest reported synthesis temperature for this compound up-to-date. This behavior was ascribed to the effects directly connected with the dopant substitution (exchange of bigger La^{3+} cation with smaller Tb^{3+}) as well as reduction of the particle size. The size effects are mostly reflected in the expansion of the cell volume, changes of the cell parameters as well as shifting and broadening of the Raman bands. Indirectly, size reduction has also an effect on the luminescence properties through the higher probability of presence of surface and net defects as well as heterogeneous distribution of the Tb^{3+} ions caused by high surface-to-volume ratio. The prepared nanophosphors show basically green emission with exception of white-green in case of the $LaInO_3$:Tb^{3+}. Strong emission quenching was found in the latter case being most likely a consequence of the nonradiative energy transfer between Tb^{3+} and In^{3+} as well as the presence of defects. In comparison to the Pechini's method, the $LaXO_3$ nanoparticles required significantly lower annealing temperature (700 °C) necessary for complete crystallization. Generally the resulting particles are distinctly smaller (5 to 25 nm) and less agglomerated (50−100 nm) depending on the reaction conditions as well as thermal treatment. For the first time, it was shown that the $LaGaO_3$:Tb^{3+} nanopowder has crystallized in the high-temperature rhombohedral $R\bar{3}c$ phase.

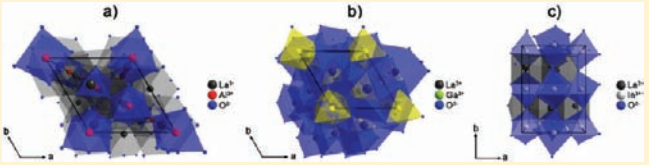

INTRODUCTION

Advanced development and engineering of the perovskite nanoparticles, described by the general chemical formula ABO_3 (where A is a cation usually in the +1, +2, or +3 oxidation state and B in the +5, +4 or +3, respectively), opens a variety of new possibilities in the field of modern optics,[1−3] electronics,[4,5] and energy conversion[6,7] applications. Recently $LaXO_3$ based perovskites (where X refers to Al^{3+}, Ga^{3+}, and In^{3+}) have attracted attention because of their potential use as a substrate for solid oxide fuel cells[6] as well as a promising host material for phosphor application.[3,8−10] Doping of the $LaXO_3$ with divalent cations such as Sr^{2+} or Mg^{2+}, especially $LaGaO_3$ and $LaInO_3$, leads to dramatic increase of the conductivity being extremely important in SOFC[6] while modification with trivalent rare earth cations (Eu^{3+}, Tb^{3+}, Nd^{3+}) or d-metals (Cr^{3+}, Bi^{3+}) leads to efficient luminescence.[3,8,11]

Ideal ABO_3 perovskite has a cubic structure with $Pm\bar{3}m$ symmetry. However, $LaAlO_3$ is rhombohedral with centrosymmetric space group $R\bar{3}c$. The lanthanide cation occupies a crystallographic site with D_3 point symmetry coordinated by 12 oxygen ions. The $LaAlO_3$ single crystal undergoes phase transition into the $Pm\bar{3}m$ cubic phase at 800 K.[12,13] Both $LaGaO_3$ and $LaInO_3$ have orthorhombic distortion. The crystal structure consists of tilted, slightly distorted, corner connected GaO_6 or InO_6 octahedra. Rare earth cations are in 8-fold coordination possessing the C_s point symmetry.[8,14,15] The $LaGaO_3$, at room temperature, adopts the centrosymetric space group *Pbnm* and transforms into the rhombohedral $R\bar{3}c$ phase at 423 K.[16,17] The centrosymetric ***Pnma*** space group was assigned to the $LaInO_3$ single crystal,[18] and there is no literature data regarding its phase transformation.

It is interesting to note changes of the $LaXO_3$ band gap energy in the Group 13 series (Al^{3+}, Ga^{3+}, and In^{3+}). For instance, the $LaAlO_3$ is considered as a typical dielectric material with band gap energy ≈5−6 eV.[19] However, complete Ga^{3+} substitution at the B site leads to the semiconducting compound characterized by wide band gap with energy of 3.74 eV.[20,21] Furthermore, replacement of the B cation with In^{3+} results in formation of a narrow band gap semiconductor with band gap of 2.2 eV.[18] Consequently both semiconducting materials, after proper activation with optically active rare earth ions (Eu^{3+}, Tb^{3+}, Ce^{3+}), should in turn deliver attractive phosphors for field emission displays (FEDs), electroluminescent displays (EDs), plasma

Received: November 30, 2010
Published: March 03, 2011

display panels (PDPs), or vacuum fluorescent displays (VFDs). It was shown that the best candidates for such applications are materials showing reasonable intrinsic conductivity allowing for ease of charge dissipation.[3,8] As a matter of fact, dielectric $LaAlO_3$ cannot be even taken under consideration for display technology since it will collect significant charge at its surface during cathode-ray exposition.[22] Nonetheless, the $LaAlO_3$ can be used as a host material for other full-color phosphor applications, as it was shown by Deren et al.[9,10,13]

According to our knowledge there are only few articles published on the synthetic routes to $LaAlO_3:Tb^{3+}$,[10] $LaGaO_3:Tb^{3+}$,[23,24] and $LaInO_3:Tb^{3+3}$ nanophosphors all based on the well-known Pechini's method. In the present contribution, our efforts were focused on the nonhydrolytic synthesis (Bradley reaction) of the $LaXO_3$ (X = Al^{3+}, Ga^{3+}, and In^{3+}) nanoparticles doped with trivalent terbium ions. Recently we have successfully adopted the same technique in preparation of the $LaAlO_3:Nd^{3+}$ nanoparticles.[25] As it was shown, the chosen approach allows for thorough control over stoichiometry of designed systems, and particle size tuning with reduced agglomeration. The detailed studies of structural and luminescence properties were performed and rationalized in relation to existing concepts.

EXPERIMENTAL SECTION

All manipulations with the metal alkoxides were carried out using Schlenk techniques in a dry nitrogen atmosphere. The X-ray diffraction (XRD) patterns were collected in a 2Θ range of 5−120° with X'Pert PRO X-ray diffractometer (Cu, $K\alpha_1$: 1.54060 Å) (PANalytical). The $LaXO_3$ (X = Al^{3+}, Ga^{3+}, and In^{3+}) nanoparticles were investigated by high resolution transmission electron microscopy (HRTEM) using a Philips CM-20 Super Twin microscope, operating at 200 kV. Samples for HRTEM were prepared by dispersing a powder in methanol and leaving a droplet of the suspension on a copper microscope grid covered with perforated carbon. Elemental analysis was carried out using a SEM-EDS Hitachi TM 1000-μDeX Tabletop Microscope performing 10 measurements from different random areas for each sample. Raman spectroscopy was done utilizing a LabRam HR 800 Horiba Jobin Yvon equipped with a 9 mW HeNe laser emitting 632.8 nm line. Excitation spectra were recorded with a Spectra Pro 750 monochromator, equipped with Hamamatsu R928 photomultiplier. As an excitation source a 450 W xenon arc lamp was coupled with a 275 nm excitation monochromator. The luminescence spectra were recorded using a Jobin Yvon THR 1000 monochromator equipped with a Hamamatsu R928 photomultiplier and a 1200 grooves/mm holographic grating. As an excitation source, the continuous 266 nm line of the third harmonic of a $YAG:Nd^{3+}$ laser was used. The luminescence decay times were measured utilizing a LeCroy Wave Surfer oscilloscope after 266 nm excitation with the $YAG:Nd^{3+}$ laser operating at a 10 ns pulse mode. All recorded spectra were corrected according to the apparatus' characteristics.

Synthesis of $LaAlO_3:Tb^{3+}$ Nanoparticles. To prepare the $LaAlO_3$ nanoparticles doped with 2 mol % of Tb^{3+}, 0.2735 g (0.862 mmol) of $La(O^iPr)_3$ (99.9% Alfa Aesar), 0.18 g (0.88 mmol) of $Al(O^iPr)_3$ (99.99% Alfa Aesar), and 1.57 mg (0.00344 mmol) of $Tb(acac)_3$ (99.9% Alfa Aesar) were dissolved in 25 mL of acetophenone (99% Sigma Aldrich), resulting in transparent yellow solution at room temperature. The prepared solution was refluxed at 202 °C for 8 h until turbid yellow suspension was formed. The final product was separated by high speed centrifugation and further washed six times with 10 mL portions of ethanol for removal of acetophenone. Afterward, the particles were resuspended in absolute ethanol and dried using a vacuum evaporator. Additional thermal treatment at 700 °C for 8 h was applied to improve the crystallinity of the particles.

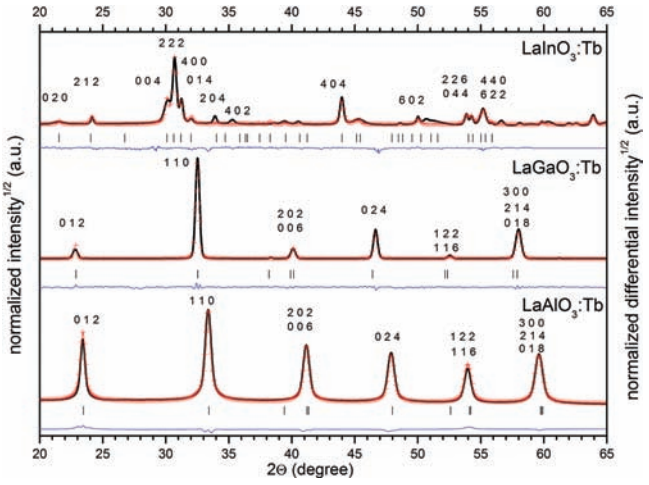

Figure 1. XRD patterns (black lines) and results of the Rietveld analysis (red, fitted diffraction; blue, differential patterns; column, reference phase peak position) of the $LaXO_3:Tb^{3+}$ nanoparticles.

Synthesis of $LaGaO_3:Tb^{3+}$ Nanoparticles. For preparation of the $LaGaO_3$ nanoparticles doped with 2 mol % of Tb^{3+}, 0.273 g (0.862 mmol) of $La(O^iPr)_3$, 0.27 g (0.88 mmol) of $Ga(O^iPr)_3$ (99% Alfa Aesar), and 8 mg (0.0175 mmol) of $Tb(acac)_3$ were dissolved in 50 mL of acetophenone, resulting in a transparent yellow solution at room temperature. The next preparation steps were essentially the same as in the $LaAlO_3:Tb^{3+}$ synthesis. The post-treatment at 700 °C for 8 h was applied to improve the crystallinity of the final product.

Synthesis of $LaInO_3:Tb^{3+}$ Nanoparticles. The preparation procedure of $LaInO_3$ nanoparticles doped with 2 mol % of Tb^{3+} involved 0.2735 g (0.862 mmol) of $La(O^iPr)_3$, 0.239 g (0.176 mmol) of $In_3O(O^iPr)_{13}$ (99.9% Multivalent), and 8 mg of $Tb(acac)_3$. All reactants were dissolved in 50 mL of acetophenone, and the same steps were repeated as in the latter syntheses. The post-treatment annealing was applied (700 °C for 8 h) to improve the crystallinity of the product.

RESULTS AND DISCUSSION

Structural Analysis. The structure evolution of the $LaXO_3$ (X = Al^{3+}, Ga^{3+}, and In^{3+}) doped with 2 mol % of Tb^{3+} crystalline phases was followed by the XRD measurements. The $LaAlO_3$, $LaGaO_3$, and $LaInO_3$ samples, isolated from the reaction mixture and further purified, remained essentially amorphous according to the XRD. However, after the thermal treatment at 700 °C, powders revealed detectable crystallinity (see Figure 1). All of the reflections appearing on the diffraction patterns were indexed and assigned to the rhombohedral $LaAlO_3$[26] and $LaGaO_3$[27] as well as orthorhombic $LaInO_3$[28] phases. No other secondary phases or impurities were detected confirming formation of the designed compounds series.

The cell parameters were calculated with the help of Rietveld analysis[29] using the anisotropic approach,[3031] in Maud 2.0 software[32] and further compared with the reference data (Table 1). Projections of the structures of obtained materials along *c*-axis are shown in Figure 2.

According to the existing knowledge the coordination number of La^{3+} in the $LaAlO_3$ is 12; thus, the ionic radius of La^{3+} is 1.5 Å.[33] The aluminum cation is in 6-fold coordination with cationic radius of 0.675 Å. The coordination number of lanthanum(III) is 8 in $LaGaO_3$ and $LaInO_3$ resulting then in an ionic radius of 1.3 Å. The Ga^{3+} and In^{3+} have both coordination numbers of

dx.doi.org/10.1021/ic102386e |Inorg. Chem. 2011, 50, 2966–2974

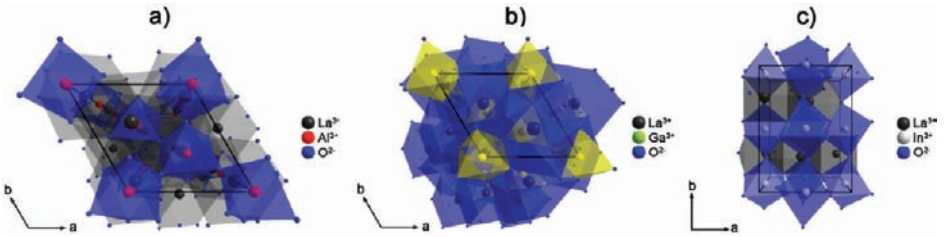

Figure 2. Projection of the $LaAlO_3$ (a), $LaGaO_3$ (b), and $LaInO_3$ structures along *c*-axis.

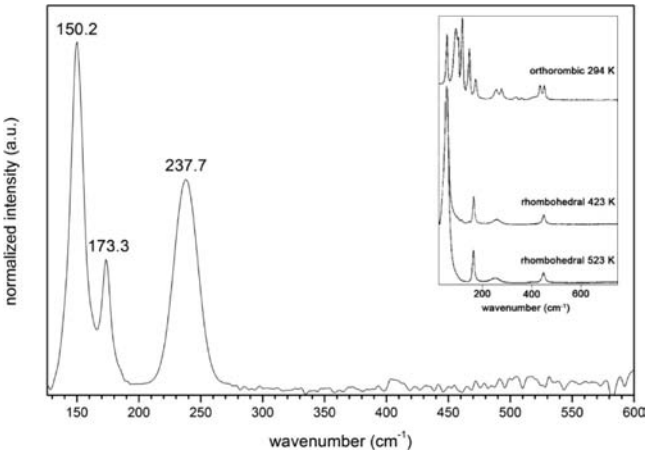

Figure 3. Raman spectra of the $LaGaO_3$:Tb^{3+} (inset reproduced under permission[39]).

6 like Al^{3+} in $LaAlO_3$ with ionic radii of 0.76 Å and 0.94 Å, respectively.[33] The coordination numbers higher than 9 are not known for Tb^{3+} in oxides. The most preferred Tb^{3+} coordination is 8 with corresponding ionic radius of 1.18 Å.[33] Thus, it was generally assumed that, in series of the $LaXO_3$ compounds, Tb^{3+} ions are replacing La^{3+} positions since their ionic radii are most compatible. Moreover, it is expected that introduction of smaller Tb^{3+} ions would cause some distortion of the crystal symmetry. As it was shown in case of $LaAlO_3$, the complete substitution of La^{3+} with Tb^{3+} leads to formation of the $TbAlO_3$ with *Pbnm* orthorhombic symmetry rather than rhombohedral $R\bar{3}c$ being a consequence of the substituting ion size and its coordination number.[34] However, taking into account Rietveld analysis, substitution of La^{3+} with 2 mol % of Tb^{3+} in the $LaAlO_3$ did not change the symmetry of the crystal, and best fitting was obtained with $R\bar{3}c$. No structure changes were noticed for the $LaInO_3$ sample which remained orthorhombic with symmetry group depicted as *Pnma* as it was expected. The Tb^{3+} doping causes most significant differences in $LaGaO_3$. Generally $LaGaO_3$ crystallizes in *Pbnm* symmetry with phase transition to $R\bar{3}c$ at 423 K, and La^{3+} is in 8-fold coordination like in the case of $LaInO_3$. It was suggested that the cell parameters of the $LaGaO_3$ could be easily tuned by the change of the smaller than La^{3+} other rare earth ions (RE^{3+}) in single crystal. Therefore, we observed that the replacement of the La^{3+} with isovalent Tb^{3+} results in stabilization of the rhombohedral $R\bar{3}c$ phase instead of formation of the orthorhombic one at doping level of 2 mol % of Tb^{3+}. This conclusion was supported by the fact that the Rietveld fitting with $R\bar{3}c$ symmetry gave much better correspondence with experimental data than *Pbnm* where the magnitude of error was too significant to be acceptable. These phenomena were explained earlier by the fact that phase transitions should be governed by the ionic size of the lanthanide ions in different types of host materials.[35,36] However, this goal was not ever achieved for the high RE^{3+} doping level up to 20 mol % in single crystals.[37] Additionally, even in works of Liu et al.,[23,24] focused on studies of RE^{3+} doped $LaGaO_3$ systems constituted of 60 nm particles, there are no reports regarding formation of the rhombohedral phase.

It is well-known that XRD is a good technique to probe a global structure of crystallites.[38] However it is not sensitive enough technique to study the amount of the secondary phases or impurities if the total content of each of them is below 5% of the total. Thus to get more in-depth information regarding local structure, to check the possible presence of residual impurities, and finally to support the formation of the rhombohedral phase of the $LaGaO_3$:Tb^{3+}, the Raman spectra were taken at room temperature for $LaGaO_3$:Tb^{3+} (see Figure 3). It is well-known that if the $LaGaO_3$ forms the orthorhombic *Pbnm* phase, 24 Raman active modes should be observed. Hence the Raman spectra present an abundance of bands. In case of the rhombohedral $R\bar{3}c$ structure only 5 Raman modes are active, and the spectra are drastically simplified.[39] According to the data presented by Tompsett et al.[39] one can distinguish characteristic modes at 150.2 cm^{-1}, 173.3 cm^{-1}, and 237.7 cm^{-1} corresponding to the rhombohedral $LaGaO_3$. Additionally, all bands are slightly shifted and broadened, but the Raman spectra are essentially the same as for the reference crystal. These effects are commonly ascribed to the size reduction of crystallites directly affecting force constants and vibration amplitudes of the nearest neighboring bonds.[40] Xu et al.[41] provided another explanation showing that phonon dispersion in systems constituted of nanoparticles is the main mechanism responsible for asymmetric broadening and shift of the Raman bands. Moreover, relation of the bands' intensities is quite different, especially the mode at 237.7 cm^{-1}, in comparison to that in the single crystal. This change might be caused by random orientation of the $LaGaO_3$:Tb^{3+} nanocrystallites since the single crystal was oriented along a fixed direction.[39] From the point of view of phosphor applications, the occurrence of the $LaGaO_3$ phase transition at such low temperature is the main limitation of its use in this field because of the twinning of the orthorhombic $LaGaO_3$ single crystal during phase transformation. Thus, the synthesis of $LaGaO_3$ nanoparticles leading directly to the high-temperature rhombohedral phase appears beneficial.[42]

The cell parameters were compared to the reference data (see Table 1). However, observed differences are on one hand a result of replacing the bigger La^{3+} ions with smaller Tb^{3+} and thus expected shrinking of the cell volume. On the other hand, the well-known grain size effect may contribute to the calculated values causing additional expansion of the cell volume.[43,44] Thus

Table 1. Cell Parameters of the $LaXO_3:Tb^{3+}$ Nanoparticles

sample	cell parameters (**sample**/reference[a])	space group	mean crystallite size Rietveld/Scherrer (nm)
$LaAlO_3:Tb^{3+}$	a = **5.373(4)** Å/5.364(8) Å	$R\bar{3}c$	20.0 ± 0.1/18 ± 0.4
	c = **13.116(1)** Å/13.111(3) Å		
	V = **327,969(7)** Å^3/326.8 Å^3		
$LaGaO_3:Tb^{3+}$	a = **5.521(7)**Å/5.574(5) Å	$R\bar{3}c$	55.8 ± 0.1/24 ± 0.6
	c = **13.456(3)**Å/13.56(5) Å		
	V = **355.305(5)** Å^3/365.08 Å^3		
$LaInO_3:Tb^{3+}$	a = **5.958(8)** Å/5.9404(1) Å	*Pnma*	25.3 ± 0.1/20 ± 0.7
	b = **8.326(0)** Å/8.215(8) Å		
	c = **6.023(4)** Å/5.722(9) Å		
	V = **298.838(8)** Å^3/279.31 Å^3		

[a] Reference crystallographic data: $LaAlO_3$,[46] $LaGaO_3$,[47] and $LaInO_3$.[48]

it appears that both phenomena are involved at the same time. Summarizing, generally all parameters vary significantly when compared to the reference materials, and their changes are due to the earlier mentioned dopant and grain size effect at nanoscale.

The mean size of crystallites was estimated from the broadening of the diffraction peaks using well know Scherrer's formula[45] and compared with values obtained from Rietveld analysis (see Table 1).

In case of Scherrer method the $LaAlO_3:Tb^{3+}$ nanoparticles' crystallite size (18 nm) was calculated as an averaged value obtained from consideration of three nonsplit peaks assigned to the following crystallographic planes 012, 110, and 024, respectively. The $LaGaO_3:Tb^{3+}$ nanoparticles' size (24 nm) was estimated taking into account 112 and 004 reflections. In the case of the $LaInO_3:Tb^{3+}$ sample only the peak ascribed to the 404 crystallographic direction was useful for estimation of the crystallite size (20 nm) since that reflection had sufficient intensity and did not overlap with the other ones. One can note that the calculated mean grain size vary strongly with the type of the material as well as the method of the size estimation. The Sherrer's based average grain size is showing the primary size of particles which is consistent with the size evaluated from TEM images (see Figure 4). Nevertheless the general trend is the same meaning that independently on the approach the $LaAlO_3:Tb^{3+}$ nanoparticles are the smallest ones whereas $LaGaO_3:Tb^{3+}$ powders the largest.

In accordance with the TEM studies (see Figure 4) the samples contain weakly agglomerated and irregular particles with primary size from 10 to 25 nm in case of $LaAlO_3:Tb^{3+}$ and 30 to 60 nm for $LaGaO_3:Tb^{3+}$ (Figure 4a and 4c). The particles are elongated and form complex, branched structures reminiscent of rice grain-like particles in both cases. Analysis of the SAED pattern reveals the presence of well developed spotty rings at positions expected for rhombohedral $LaAlO_3$ and $LaGaO_3$ (Figure 4b and 4d). The microstructure of the $LaInO_3:Tb^{3+}$ nanoparticles heated at 700 °C is shown in Figure 4e. In contrast to the former particles, morphology of the $LaInO_3:Tb^{3+}$ is very different, possibly indicating the structural differences among materials. The sample contains more regular crystalline particles forming small aggregates (50 nm) with primary size of particles 10−30 nm. The crystallization of the $LaInO_3:Tb^{3+}$ nanoparticles at such low temperature could be explained in terms of energy conditions for crystallization. Lower effective charge for the bigger In^{3+} cations results, apparently, in their easier diffusion in the oxide structure, which facilitates the crystallization kinetics. Smaller size difference between the La and In cations is apparently also facilitating thermodynamically the formation of the less densely packed and less symmetric orthorhombic structure. The crystallite size of the particles was essentially smaller than that of the particles produced by the Pechini technique (usually 60 nm) being in the range of 17 to 24 nm depending on the synthesized compound. Additionally all samples showed distinctly lower particles agglomeration which might be of significant interest for biologically related applications.

The SAED image (see Figure 4f) showed well resolved rings and spots corresponding to the orthorhombic $LaInO_3$. The presence of an amorphous phase (shell) was noticed in TEM and SAED patterns in all cases as well. It is noteworthy that only $LaInO_3:Tb^{3+}$ samples revealed detectable crystallinity directly after the synthesis without need in additional thermal treatment (see insets in Figure 4e and 4f), whereas both $LaAlO_3:Tb^{3+}$ and $LaGaO_3:Tb^{3+}$ remained amorphous under the same reaction conditions. The $LaInO_3:Tb^{3+}$ heat-treated at 700 °C contains loosely aggregated, regular particles surrounded by amorphous phase with grain size varying from 3 to 5 nm. As a matter of fact, the presence of an amorphous shell around the crystalline core is a typical feature of the nonhydrolytic preparation routes. The mechanism relies on nucleation of the particles through formation of ordered polyoxometallate species terminated on their surface by the organic ligands. Elimination of the latter leads directly to the formation of an amorphous shell.[49,50]

The Tb^{3+} content in the $LaXO_3$ (X = Al^{3+}, Ga^{3+}, In^{3+}) was checked by energy dispersive spectroscopy (EDS) analysis (see Figure 5) for samples with 2 mol % of dopant as well as for a series with Tb^{3+} concentrations varying from 2 mol % to 5 mol %. The resulting content of the Tb^{3+} ions was higher than the desired (2.4 mol %) in all cases but remained constant within the series of prepared materials. The elevated content of Tb^{3+} could be caused by several factors. On one hand it is likely that there is a variation in distribution of the optically active ions in the matrix resulting in the presence of richer dopant content in the close-to-surface area since surface to volume ratio is higher in nanoparticles than in a bulk material. On the other hand, the source of such elevation in dopant content could be sought in the principles of the EDS technique, where results are dependent on the penetration depth of the beam. [51] Nevertheless, the observed deviations are within the statistical standard margin of the EDS analysis.

Optical Properties. Luminescence spectra of the $LaXO_3$ (X = Al^{3+}, Ga^{3+}, In^{3+}) doped with 2 mol % of Tb^{3+} and sintered at 700 °C were measured at 300 and 77 K (see Figure 6). All

dx.doi.org/10.1021/ic102386e |*Inorg. Chem.* 2011, 50, 2966–2974

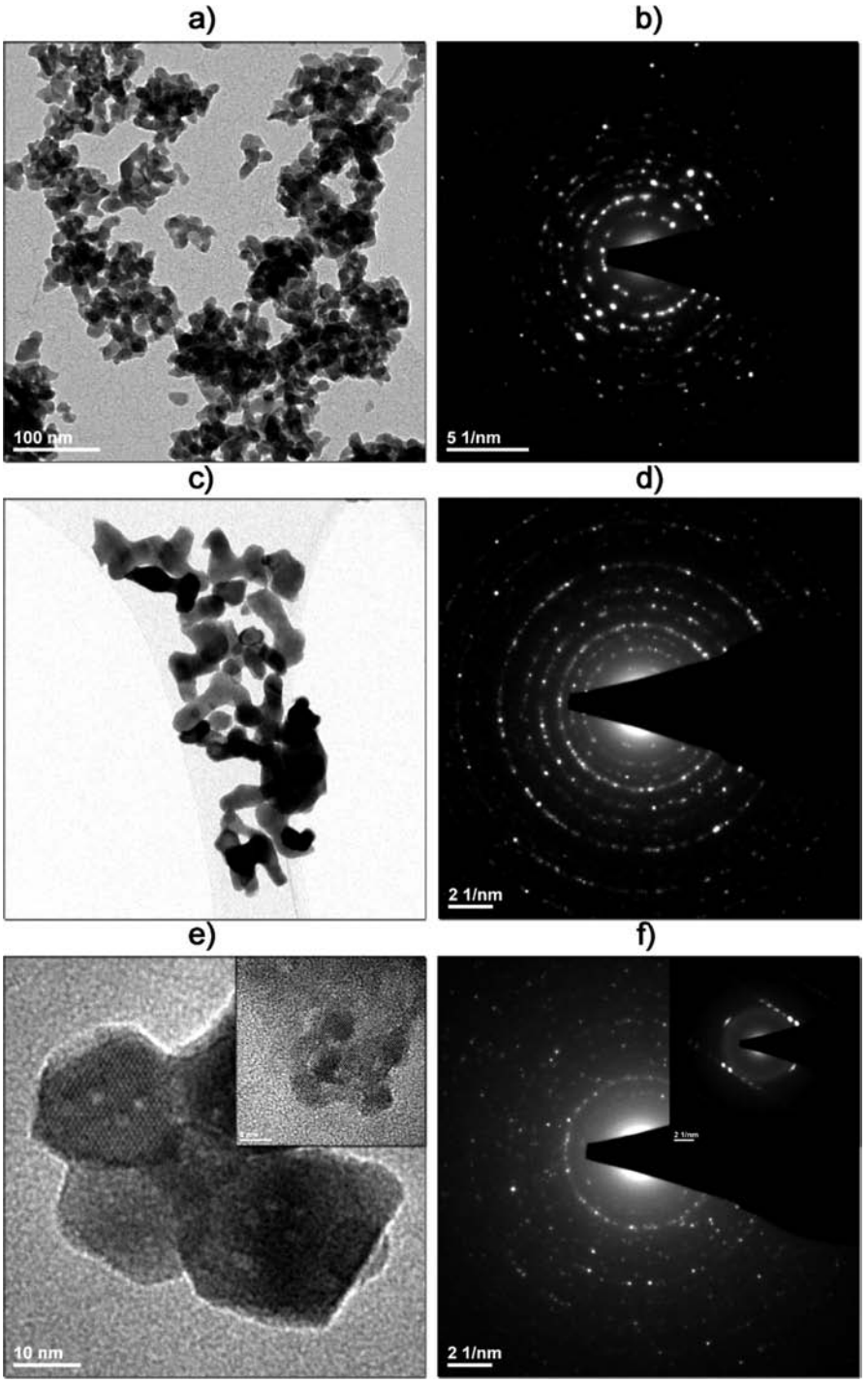

Figure 4. TEM images of the (a) $LaAlO_3$, (c) $LaGaO_3$, (e) $LaInO_3$ and SAED images of the (b) $LaAlO_3$, (d) $LaGaO_3$, and (f) $LaInO_3$ heated at 700 °C. Insets in (e) and (f) show $LaInO_3$ sample after synthesis.

recorded spectra were normalized to the maximum value of intensity. The observed lines originate from the de-excitation of the $^5D_4$ emitting level into the crystal field components of the $^7F_{6-0}$ levels of the ^7F ground term. The $^5D_4 \rightarrow {}^7F_6$ transition is located at 492 nm (20325 cm^{-1}), $^5D_4 \rightarrow {}^7F_5$ at 542 nm (18450 cm^{-1}), $^5D_4 \rightarrow {}^7F_4$ at 588 nm (17068 cm^{-1}), and $^5D_4 \rightarrow {}^7F_3$ at 621 nm (16 103 cm^{-1}), respectively. The transitions associated with lower energies, such as $^5D_4 \rightarrow {}^7F_{2-0}$, had low intensity and were scarcely detected. It is well-known that the emission properties of Tb^{3+} strongly depend on the content of the optically active ions. Therefore, usually when the concentration of Tb^{3+} is less than 0.5 mol %, the emission assigned to the $^5D_3 \rightarrow {}^7F_J$ electron transition can be observed at the blue spectral region covering the range of 350−470 nm. [52,53] However, if the critical value of dopant concentration is exceeded, the blue emission disappears because of the cross relaxation processes, [54] which is also the case in this study (Tb^{3+} content around 2 mol %). Hence we limited the spectral region to the most interesting range of 450−700 nm.

dx.doi.org/10.1021/ic102386e |*Inorg. Chem.* 2011, 50, 2966–2974

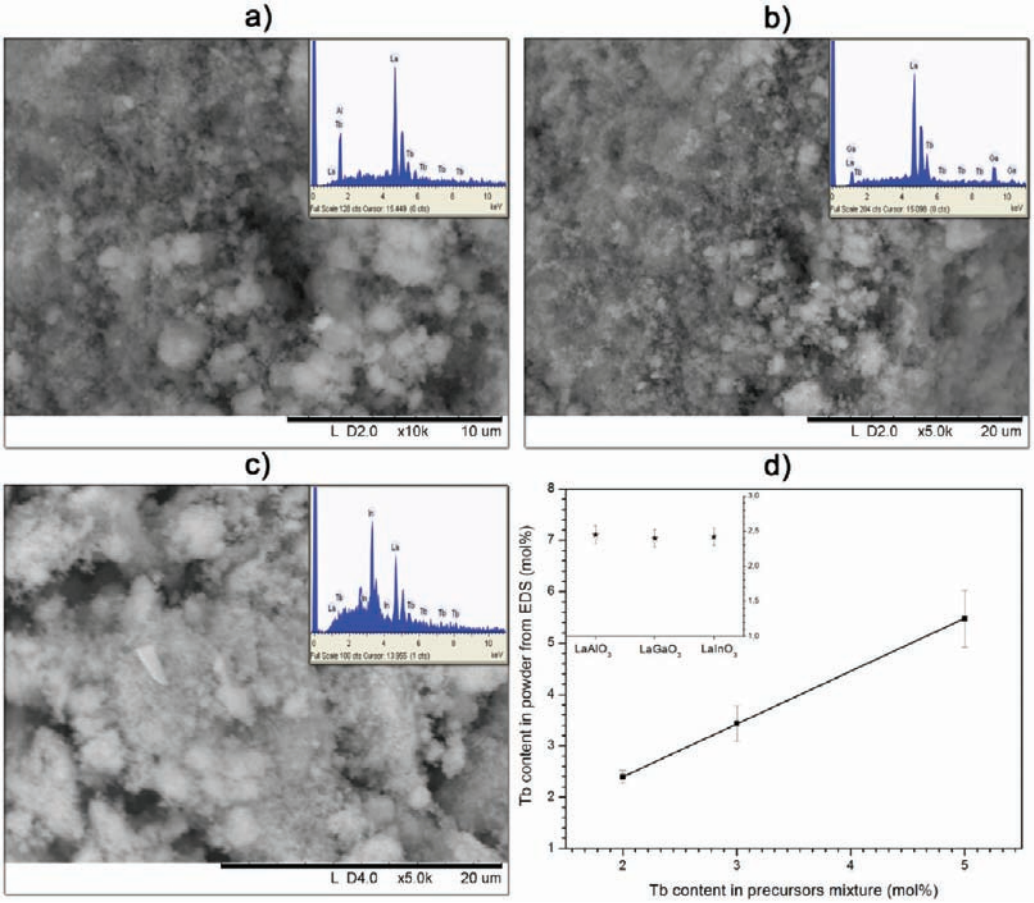

Figure 5. SEM-EDS characterization of the $LaAlO_3$:Tb^{3+} (a), $LaGaO_3$:Tb^{3+} (b), $LaInO_3$:Tb^{3+} (c), and content of the Tb^{3+} in the final materials (d).

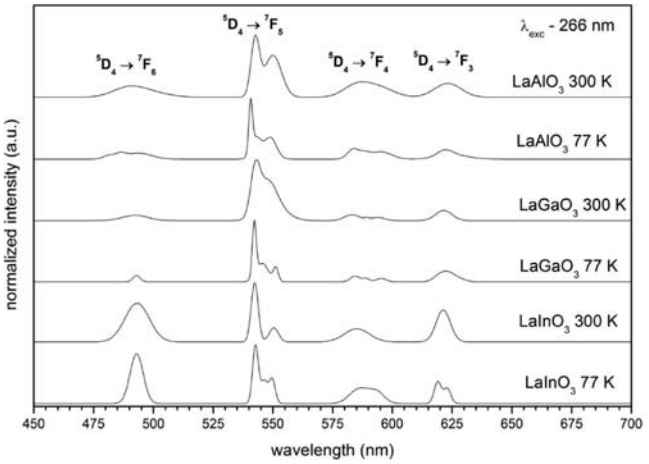

Figure 6. Luminescence spectra of the $LaXO_3$:Tb^{3+} recorded at 300 and 77 K.

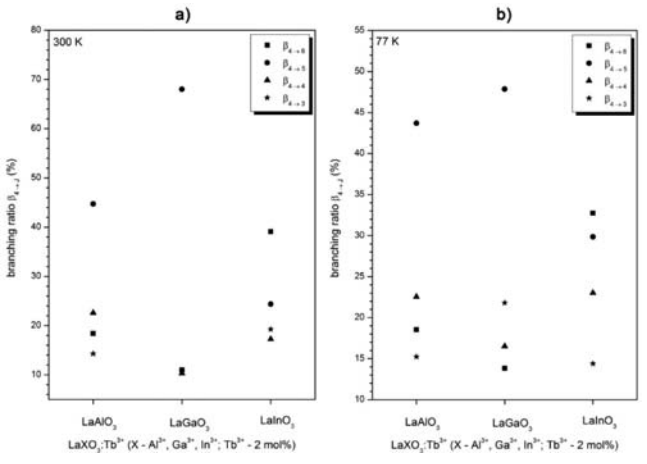

Figure 7. Branching ratio $\beta_{4\rightarrow J}$ of the $LaXO_3$:Tb^{3+} (X = Al^{3+}, Ga^{3+}, In^{3+}) nanoparticles sintered at 700 °C.

Qualitatively the $LaAlO_3$:Tb^{3+} system exhibits the strongest emission in comparison to that of the other two tested compounds. The intensity of the green emission in $LaGaO_3$:Tb^{3+} is slightly weaker but comparable with that of $LaInO_3$:Tb^{3+}. As a matter of fact, the observed luminescence behavior of $LaAlO_3$ and $LaGaO_3$ nanoparticles doped with Tb^{3+} is closely related to each other. Comparable number, shape, and intensity of the bands is observed. This indicates that the Tb^{3+} ions are located in similar crystallographic positions in host materials since both compounds are crystallizing in the same $R\bar{3}c$ symmetry. Even though some differences can be noted as well, that is, slight variation of the bands intensity most likely indicating more covalent character of the $LaGaO_3$ as compared to the $LaAlO_3$ (in the view of higher electronegativity of gallium 1.81, compared

dx.doi.org/10.1021/ic102386e |*Inorg. Chem.* 2011, 50, 2966–2974

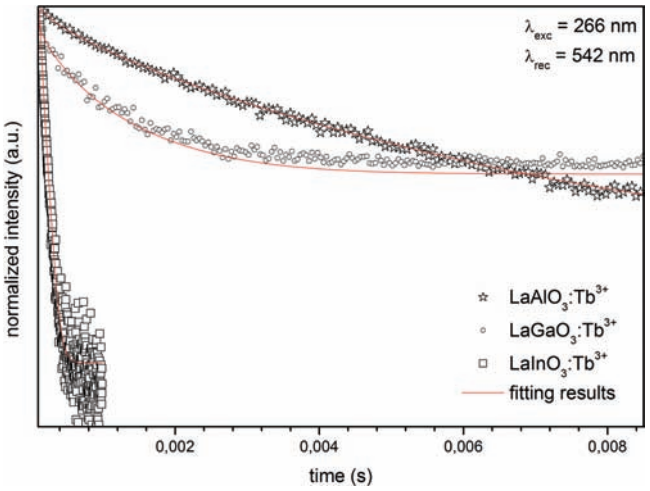

Figure 8. Decay profiles of the $LaXO_3:Tb^{3+}$ nanoparticles recorded at room temperature.

to aluminum 1.61). However, the $LaInO_3:Tb^{3+}$ emission shows distinctly different behavior. On one hand, it can clearly be seen that the de-excitation energy is distributed in a different manner resulting from incorporation of the Tb^{3+} into a position with lower symmetry. On the other hand, still the most intense transition is $^5D_4 \rightarrow {}^7F_5$ but the color of emitted light is white with a pale green glow in contrast to the intensive green luminescence of the $LaAlO_3:Tb^{3+}$ and $LaGaO_3:Tb^{3+}$ nanoparticles, respectively.

The branching ratio $\beta_{4\rightarrow J}$ for the $^5D_4 \rightarrow {}^7F_J$ transitions (see Figure 7) allows for estimation of the energy distribution to the particular emission channels and could be directly calculated from the emission spectra[55] using the following formula:

$$\beta_{4-J} = \frac{I(^5D_4 \rightarrow {}^7F_x)}{\sum_J I(^5D_4 \rightarrow {}^7F_J)}$$

where the numerator is the integrated intensity of the respective electron transition from $^5D_4$ excited level to the one of each ^7F ground levels and the denominator describes a sum of integrated intensities over all transitions.

A comparison of the $\beta_{4\rightarrow J}$ indicates a different distribution of the de-excitation energy in the samples. It can clearly be seen that almost 70% of the total energy is emitted through the magnetic $^5D_4 \rightarrow {}^7F_5$ electron transition. The remaining energy is evenly distributed through the rest of the emission channels, that is, $^5D_4 \rightarrow {}^7F_6$, F_4, and F_3 (10% for each), resulting in a deeper green emission for the $LaGaO_3:Tb^{3+}$. However, for the $LaAlO_3:Tb^{3+}$ system 20% less energy is emitted through the $^5D_4 \rightarrow {}^7F_5$ (44%) transition, whereas the rest of the energy is unevenly split between the $^7F_6$ (18%), $^7F_4$ (24%), and $^7F_3$ (14%) channels respectively. Hence the resulting color of the $LaAlO_3:Tb^{3+}$ emission is slightly 'less' green than that of $LaGaO_3:Tb^{3+}$. However, green with white glow was recorded for the $LaInO_3:Tb^{3+}$ nanoparticles being a consequence of the color mixing with comparable intensity of the $^7F_6$ (light blue, 39%), $^7F_5$ (green, 24%) and $^7F_3$ (red, 19%) transition bands. In fact, such energy distribution is a direct consequence of the structural variety in the $LaXO_3:Tb^{3+}$ compounds. Most likely, the less distorted rhombohedral structure of the $LaGaO_3$, upon substitution with Tb^{3+}, results in more green luminescence than in case of the $LaAlO_3$ with identical symmetry. However, one would expect

Table 2. Effective Luminescence Lifetimes of the $LaXO_3:Tb^{3+}$ Samples Measured at 300 and 77 K

	effective luminescence lifetime τ_m (ms)	
sample	77 K	300 K
$LaAlO_3:Tb^{3+}$	3.07 ± 0.15	2.9 ± 0.145
$LaGaO_3:Tb^{3+}$	2.98 ± 0.15	2.8 ± 0.14
$LaInO_3:Tb^{3+}$	0.234 ± 0.012	0.195 ± 0.01

appearance of distortions in the $LaAlO_3$ structure upon incorporation of Tb^{3+} ions forcing 8-fold coordination. Finally, the complete replacement of La^{3+} results in formation of the $TbAlO_3$ crystals with lower *Pbnm* symmetry.[34] In case of the $LaInO_3:Tb^{3+}$ nanoparticles the color of the emission is a result of different level splitting, being directly related to the symmetry of Tb^{3+} crystallographic position (C_s instead of D_3).

Results of the luminescence kinetics studies performed at 300 and 77 K (see Table 2) showed nonexponential profiles of the decay times (see Figure 8). Thus, the following equation was used for the calculation of the lifetimes:

$$\tau_m = \frac{\int_0^{\infty} tI(t)\,dt}{\int_0^{\infty} I(t)\,dt} \approx \frac{\int_0^{\tau max} tI(t)\,dt}{\int_0^{tmax} I(t)\,dt}$$

where $I(t)$ represents the luminescence intensity at time t corrected for the background, and the integrals are evaluated on a range of $0 < t < t^{max}$ where $t^{max} \gg \tau_m$.[56] The effective decay times for the $LaAlO_3:Tb^{3+}$ and $LaGaO_3:Tb^{3+}$ nanoparticles are substantially the same for both temperatures of 77 and 300 K (close to ≈3 ms). Hence it could be an indication that the structure of crystallites is essentially the same for both compounds. Therefore, it can be concluded that Tb^{3+} ions are placed in the same symmetry sites as supported by the structural data. The lifetimes recorded for the $LaAlO_3:Tb^{3+}$ showed the same nonexponential character but were shorter in comparison to the data presented by Deren et al.[10] (4.4 ms) and close to the results of Liu et al.[57] (2.66 ms).

The comparison of the kinetic data for the $LaGaO_3:Tb^{3+}$ with those of Liu et al.[23] showed that the decay times were almost two times longer, being 2.9 ms. We believe that it is mainly due to the different symmetries of the Tb^{3+} crystallographic positions resulting in distinct crystal field splitting since the $LaGaO_3$ crystallized in rhombohedral phase instead of orthorhombic one as reported in ref 23. Totally different behavior was observed for the $LaInO_3:Tb^{3+}$. The recorded decay time of 234 μs is almost six-times shorter than the reported 1.2 ms for the $LaInO_3:Tb^{3+}$ synthesized using the Pechini method.[3] The most plausible explanation could be associated with the effective energy transfer toward lattice defects. Additionally, high surface to volume ratio, being characteristic for the materials based on nanoparticles, leads to the formation of the Tb^{3+} rich surface areas resulting in emission quenching via cross relaxation mechanism. It is also probable that some clustering of the Tb^{3+} might occur contributing to the luminescence behavior as well. However, such short decay time for the $LaInO_3:Tb^{3+}$ could indicate the energy transfer to the In^{3+} ions. As it was shown by Lakshminarasimhan and Varadaju,[8] when studying optical properties of the $LaInO_3$ ceramics doped with Eu^{3+}, the energy can be dissipated via nonradiative processes. Comparison of materials prepared by different routes shows clearly that optical properties are strongly dependent on a chosen synthetic strategy.[58]

dx.doi.org/10.1021/ic102386e |*Inorg. Chem.* 2011, 50, 2966–2974

CONCLUSIONS

The $LaXO_3:Tb^{3+}$ (X = Al^{3+}, Ga^{3+}, and In^{3+}) nanoparticles were successfully produced using the Bradley reaction from alkoxide precursors. The formation of the high-temperature rhombohedral $LaGaO_3:Tb^{3+}$ phase is reported for the first time. This is of great importance in optical applications since there is no deterioration of the optical properties because of possible twinning in proximity to the phase transition temperature (423 K). Moreover, crystallization of the $LaGaO_3:Tb^{3+}$ required less energy in comparison to the product prepared by the Pechini method at 900 °C. [23] For the first time, the formation of the $LaInO_3:Tb^{3+}$ nanoparticles is reported at such a low temperature as 202 °C. However, the crystallinity of this material was strongly improved by a post annealing at 700 °C.

It was shown that the optical properties of the $LaAlO_3:Tb^{3+}$ were comparable with those of the materials reported by Deren et al.[10] whereas $LaGaO_3:Tb^{3+}$ and $LaInO_3:Tb^{3+}$ showed essentially different behavior than that reported by Liu et al.[23] Variation in optical properties was explained in terms of formation of a different phase for the $LaGaO_3:Tb^{3+}$ as well as occurrence of the energy transfer between Tb^{3+} and In^{3+} ions in the $LaInO_3:Tb^{3+}$. In fact, we did not observe any evidence of the emission of Ga^{3+} and In^{3+} in our samples indicating that the nonradiative processes were dominant in this case. The formation of the Tb^{3+} clusters is likely due to the high surface to volume ratio leading to the Tb^{3+} rich surface regions, resulting in turn in concentration quenching via a cross-relaxation mechanism. The resulting emission properties of the Tb^{3+} were also influenced by the presence of surface defects caused by adsorbed water, OH groups, and so forth. All those factors result in shortening of the lifetimes as well as reducing the efficiency of the luminescence.

We have found that the size effects are mostly reflected in the expansion of the cell volume, changes in the unit cell parameters, as well as in shifting and broadening of the Raman bands. Indirectly, the size reduction has also an effect on the luminescence properties through higher probability of surface and net defects as well as heterogeneous distribution of the Tb^{3+} ions caused by high surface-to-volume ratio.

AUTHOR INFORMATION

Corresponding Author

*E-mail: robert.pazik@kemi.slu.se (R.P.), rafal.wiglusz@int.pan.wroc.pl (R.W.).

REFERENCES

(1) Molina, P.; Ramirez, M. O.; Garcia-Sanitzo, J. V.; Alvarez-Garcia, S.; Pazik, R.; Strek, W.; Deren, P. J.; Bausa, L. E. *Appl. Phys. Lett.* **2009**, *95*, 051103.

(2) Pazik, R.; Tekoriute, R.; Hakanson, S.; Wiglusz, R.; Strek, W.; Seisenbaeva, G. A.; Gun'ko, Y. K.; Kessler, V. G. *Chem.—Eur. J.* **2009**, *15*, 6820.

(3) Liu, X.; Lin, J. *Solid State Sci.* **2009**, *11*, 2030.

(4) Sun, C.; Wang, J.; Hu, P.; Kim, M. J.; Xing, X. *Dalton Trans.* **2010**, *39*, 5183.

(5) Buscaglia, M. T.; Viviani, M.; Zhao, Z.; Buscaglia, V.; Nanni, P. *Chem. Mater.* **2006**, *18*, 4002.

(6) Lybye, D.; Poulsen, F. W.; Mogensen, M. *Solid State Ion.* **2000**, *128*, 91.

(7) Ishihara, T.; Tabuchi, J.; Ishikawa, S.; Yan, J.; Enoki, M.; Matsumoto, H. *Solid State Ion.* **2006**, *177*, 1949.

(8) Lakshminarasimhan, N.; Varadaju, U. V. *Mater. Res. Bull.* **2006**, *41*, 724.

(9) Hreniak, D.; Strek, W.; Deren, P. J.; Bednarkiewicz, A.; Lukowiak, A. *J. Alloys Compd.* **2006**, *408*−*412*, 828.

(10) Deren, P. J.; Weglarowicz, M. A.; Mazur, P.; Strek, W. *J. Lumin.* **2007**, *122*−*123*, 780.

(11) Ryba-Romanowski, W.; Gołab, S.; Dominiak-Dzik, G.; Sokólska, I.; Berkowski, M. *J. Alloys Compd.* **1999**, *284*, 22.

(12) Howard, C. J.; Kennedy, B. J.; Chakoumakos, B. C. *J. Phys.: Condens. Matter* **2000**, *12*, 349.

(13) Deren, P. J.; Krupa, J. C. *J. Lumin.* **2003**, *102*−*103*, 386.

(14) Garcia-Rubio, I.; Pardo, J. A.; Merino, R. I.; Cases, R.; Orera, V. M. *J. Lumin.* **2000**, *86*, 147.

(15) Orera, V. M.; Trinkler, L. E.; Merino, R. I.; Larrea, A. *J. Phys.: Condens. Matter* **1995**, *7*, 9657.

(16) Sandstrom, R. L.; Giess, E. A.; Gallagher, W. J.; Segmuller, A.; Cooper, E. I.; Chisholm, M. F.; Gupta, A.; Shinole, S.; Laibowitz, R. B. *Appl. Phys. Lett.* **1988**, *53*, 1874.

(17) Miyazawa, S. *Appl. Phys. Lett.* **1989**, *55*, 2230.

(18) Rogers, D. B.; Honig, J. M.; Goodenough, J. B. *Mater. Res. Bull.* **1967**, *2*, 223.

(19) Vali, R. *Comput. Mater. Sci.* **2008**, *44*, 779.

(20) de Souza, R. A.; Maier, J. *Phys. Chem. Chem. Phys.* **2003**, *5*, 740.

(21) Ogisu, K.; Ishikawa, A.; Shimodaira, Y.; Takata, T.; Kobayashi, H.; Domen, K. *J. Phys. Chem.* **2008**, *112*, 11978.

(22) Leskela, M. *J. Alloys Compd.* **1998**, *275*−*277*, 702.

(23) Liu, X.; Pang, R.; Quan, Z.; Jang, J.; Lin, J. *J. Electrochem. Soc.* **2007**, *154*, J185.

(24) Liu, X.; Lin, J. *J. Mater. Chem.* **2008**, *18*, 221.

(25) Pazik, R.; Seisenbaeva, G. A.; Gohil, S.; Wiglusz, R.; Kepinski, L.; Strek, W.; Kessler, V. G. *Inorg. Chem.* **2010**, *49*, 2684.

(26) Card No. 74494 ICDS, Fachinformationszentrum: Karlsruhe, 2010.

(27) Card No. 51039 ICDS, Fachinformationszentrum: Karlsruhe, 2010.

(28) Card No. 281549 ICDS, Fachinformationszentrum: Karlsruhe, 2010.

(29) Rietveld, H. M. *J. Appl. Crystallogr.* **1969**, *2*, 65.

(30) Delhez, R.; de Keijser, T. H.; Langford, J. I.; Louër, D.; Mittemeijer, E. J.; Sonneveld, E.J. In *The Rietveld Method*; Young, R. A., Ed.; Oxford Science, Oxford, United Kingdom, 1993; p 132.

(31) Luterotti, L.; Scardi, P. *J. Appl. Crystallogr.* **1990**, *23*, 246.

(32) Lutterotti, L.; Matthies, S.; Wenk, H.-R. *IUCr: Newsletter of the CPD* **1999**, *21*, 14.

(33) Shannon, R. D. *Acta Crystallogr.* **1976**, *A32*, 751.

(34) Geller, S.; Bala, V. B. *Acta Crystallogr.* **1956**, *9*, 1019.

(35) Tsukada, A.; Krockenberger, Y.; Noda, M.; Yamamoto, D.; Manske, L.; Alff, M. *Solid State Commun.* **2005**, *133*, 427.

(36) Strek, W.; Hreniak, D.; Boulon, G.; Guyot, Y.; Pazik, R. *Opt. Mater.* **2003**, *24*, 15.

(37) Dominiak-Dzik, G.; Ryba-Romanowski, W.; Gołab, S.; Berkowski, M. *Spectrochim. Acta* **1998**, *A54*, 2051.

(38) Schlag, S.; Eicke, H. F. *Solid State Commun.* **1994**, *59*, 659.

(39) Tompsett, G. A.; Sammes, N. M.; Philips, R. J. *J. Raman Spectrosc.* **1999**, *30*, 497.

(40) Choi, H. C.; Jung, Y. M.; Kim, S. B. *Vibrational Spectr.* **2005**, *37*, 33.

(41) Xu, C. Y.; Zhang, P. X.; Yan, L. *J. Raman Spectrosc.* **2001**, *32*, 862.

(42) Ryba-Romanowski, W.; Gołab, S.; Dominiak-Dzik, G.; Sokólska, I.; Berkowski, M. *J. Alloys Compd.* **1999**, *284*, 22.

(43) Palkar, V. R.; Ayyub, P.; Chattopadhyay, S.; Multani, M. *Phys. Rev. B* **1996**, *53*, 2167.

(44) Ayyub, P.; Palkar, V. R.; Chattopadhyay, S.; Multani, M. *Phys. Rev. B* **1995**, *51*, 6135.

(45) Klug, P.; Alexander, L.E. *X-ray Diffraction Procedure*; Wiley: New York, 1954.

(46) Li, W.; Pao, H. *Acta Phys. Sin.* **1993**, *42*, 605.

(47) Slater, P. R.; Irvine, J. T. S.; Ishihara, T.; Takita, Y. *J. Solid State Chem.* **1998**, *139*, 135.

(48) Min, P. H.; Joo, L. H.; Hyun, P. S.; Ill, Y. H. *Acta Crystallogr., Sect. C* **2003**, *59*, i131.
(49) Kessler, V. G. *J. Sol-Gel Sci. Technol.* **2009**, *51*, 264.
(50) Kessler, V. G.; Spijksma, G. I.; Seisenbaeva, G. A.; Hakanson, S.; Blank, D. H. A.; Bouwmeester, H. J. M. *J. Sol-Gel Sci. Technol.* **2006**, *40*, 163.
(51) Goldstein, J.; Newbury, D.; Joy, D.; Lyman, C.; Echlin, P.; Lifshin, E.; Sawyer, L.; Michael, J. *Scanning electron microscopy and X-ray microanalysis*; Springer: New York, 2007.
(52) Hreniak, D.; Strek, W.; Mazur, P.; Pazik, R.; Zabkowska-Waclawek, M. *Opt. Mater.* **2004**, *26*, 117.
(53) Berdowski, A. M.; Lammers, M. J. J.; Blasse, G. *J. Chem. Phys.* **1995**, *83*, 475.
(54) Vanvitert, L. G.; Johson, L. F. *J. Chem. Phys.* **1996**, *44*, 3514.
(55) Psuja, P.; Hreniak, D.; Strek, W. *J. Rare Earths* **2009**, *27*, 574.
(56) Nakazawa, E. *Phosphor Handbook*; CRC Press: Boca Raton, FL, 1999; p 104.
(57) Liu, X.; Yan, L.; Lin, J. *J. Phys. Chem.* **2009**, *113*, 8478.
(58) Pazik, R.; Hreniak, D.; Strek, W.; Speghini, A.; Bettinelli, M. *Opt. Mater.* **2006**, *28*, 1284.